RESEARCH

Open Access

Preparation, morphology and thermoelectric performance of PEDOT/CuI nanocomposites

Joherul Alam[1], Xiao Su[1], Hsu-Chiang Kuan[2], Shahraam Afshar Vahid[1], Kamil Zuber[1], Qingshi Meng[3], Fanzhe Meng[3], Dusan Losic[4] and Jun Ma[1*]

Abstract

Incorporating inorganic nanomaterials into a polymer matrix is one of the most effective ways to create thermoelectric performance for applications where physical flexibility is essential. In this study, flexible thermoelectric nanocomposite films were synthesized by incorporating inorganic copper iodide (CuI) nanosheets as the filler into poly (3,4-ethylene dioxythiophene): poly (styrene sulfonate) (PEDOT: PSS). The process involved the preparation of bulk CuI from precursors and, subsequently, the nanosheet synthesis by dissolving the bulk CuI in dimethyl sulfoxide (DMSO). The morphology of the nanosheets and the nanocomposite films was thoroughly examined, and the film's thermoelectric performance was evaluated using a standard thermoelectric measurement system, ZEM-3. The morphological observation revealed a triangular nanosheet geometry for CuI, with an average lateral dimension of ~33 nm. The PEDOT/CuI nanocomposite films were prepared by mixing CuI nanosheets with PEDOT: PSS through ultrasonication and filtration on a PVDF membrane. The film with 6.9 vol% of CuI nanosheets exhibited an electrical conductivity and Seebeck coefficient of 852.07 S·cm^{-1} and 14.95 μV·K^{-1}, respectively. This resulted in an enhanced power factor of 19.04 μW·m^{-1}·K^{-2}, much higher than the individual composite components. It demonstrated a trend of increasing power factor with the nanosheets up to 6.9 vol% due to improved electrical conductivity. The increase in electrical conductivity can be attributed to the screening effect induced by DMSO, which leads to a conformational change in the PEDOT chains. Furthermore, an optimal fraction of CuI nanosheets also contributes to this conformational change, further enhancing the electrical conductivity.

Keywords Nanocomposites, Thermoelectric performance, Nanosheets, Electrical conductivity
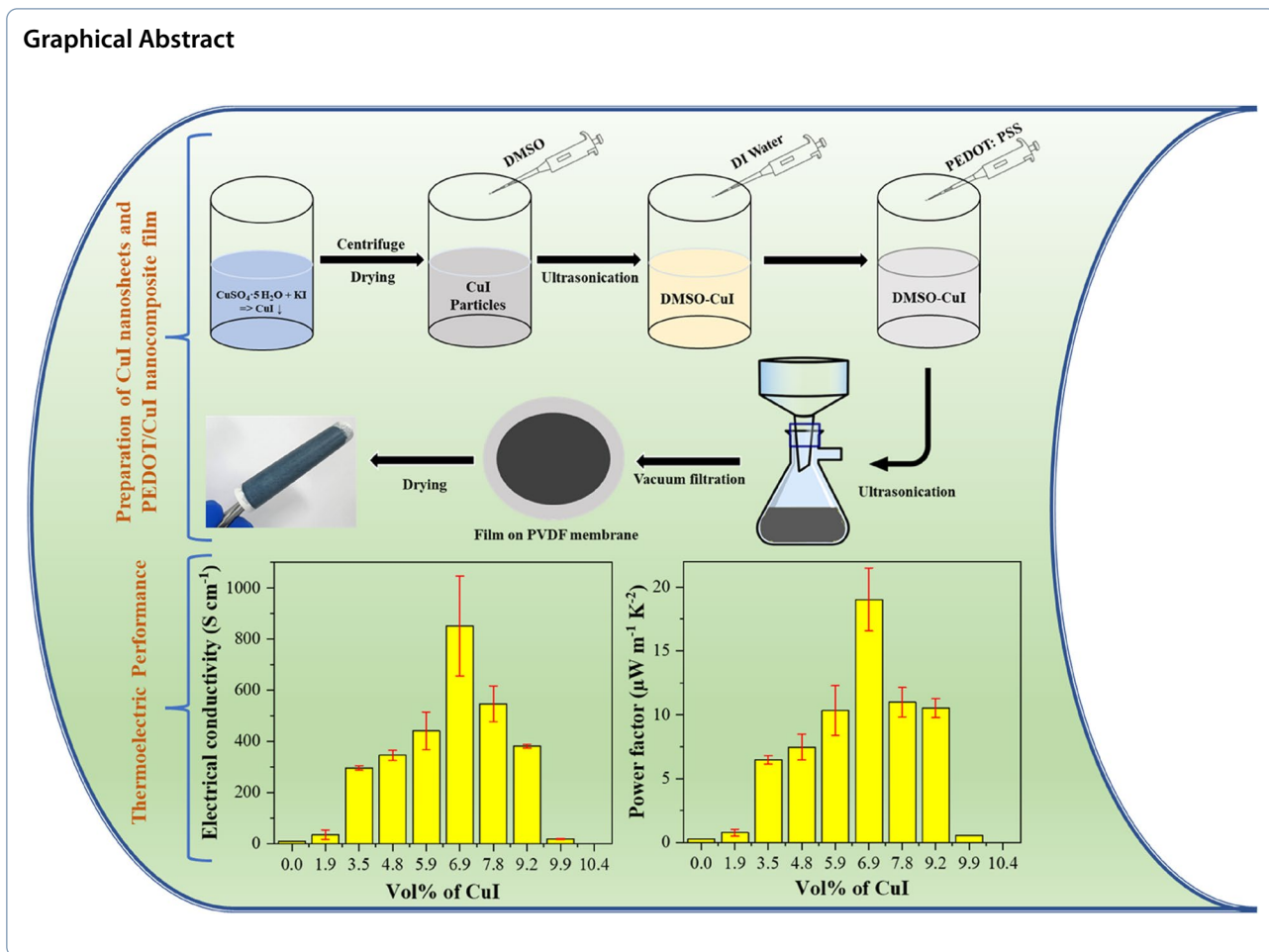
*Correspondence:
Jun Ma
Jun.Ma@UniSA.edu.au
Full list of author information is available at the end of the article

Alam *et al. Functional Composite Materials*   (2023) 4:9

Page 2 of 13

Graphical Abstract

Introduction

Since naturally available energy sources as the primary fuel are limited, several renewable technologies have been established as alternatives over the past fifty years. However, all these technologies suffer a healthy fraction of energy loss when converted to electricity, i.e., heat conduction loss. Moreover, wastage is as high as 70% due to inefficiencies in converting energy to electricity from traditional sources such as petroleum, natural gas, and coal [1, 2]. From this perspective, thermoelectric materials have the potential to recover a considerable amount of wasted energy by converting heat to electricity.

Although thermoelectric technology holds such promise, it is limited by low energy efficiency. The synthesis processes are usually complex and involve high temperatures with toxic and rare earth elements. To address these issues, many studies have been conducted to enhance thermoelectric efficiency over the last several decades, focusing on appropriate material selection, rational design, and more importantly, facile synthesis techniques for cost-effective thermoelectric materials [3].

The performance of thermoelectric materials can be realized by a unitless quantity called the Figure of merit, *ZT*. It is expressed as $(S^2\sigma/k)*T$, where *S*, σ, *k*, and *T* are the Seebeck coefficient, electrical conductivity, thermal conductivity, and absolute temperature, respectively. Organic materials and their composites typically exhibit very low thermal conductivity, and in many cases, accurate measurement is challenging. As a result, the term $S^2\sigma$, known as the power factor, is often used to evaluate the thermoelectric performance of polymer nanocomposites [4–6]. However, achieving high-performance thermoelectric materials is challenging since the Seebeck coefficient and electrical conductivity are interdependent; increasing one often results in the decrease of the other. Thus, decoupling these parameters poses a significant hurdle in developing highly efficient thermoelectric materials.

The past years have witnessed a remarkable improvement in thermoelectric materials, especially in obtaining inorganic thermoelectric materials with high *ZT* values. For example, a high *ZT* value of 2.6 has been reported in

Alam *et al. Functional Composite Materials*   (2023) 4:9

Page 3 of 13

tin selenide by Zhao et al. [7]. On the other hand, organic conducting polymers have also shown promising thermo-electric performances. They can resolve the shortcomings (e.g., being rare, expensive, and toxic) of inorganic materials. In addition, they have favorable properties of low density and cost and ease of synthesis and processing into versatile forms.

Capable of recovering low-grade waste heat, conducting polymers and their nanocomposites are often synthesized from abundant elements using low-cost manufacturing techniques. Their inherent low thermal conductivity and flexibility could pave the way for new applications and device designs. Noteworthy is that flexibility has been achieved by converting bulk semiconductor particles into nanosheets, such as antimonene and bismothene [8, 9]. Due to its outstanding electrical conductivity, PEDOT: PSS has been extensively studied not only for supercapacitors [10–12] but also for thermoelectric applications [5, 6, 13–16].

Organic/inorganic nanocomposites can potentially harness the combined benefits of two crucial components: the high electrical conductivity of conducting polymers and the elevated Seebeck value of inorganic thermoelectric materials, resulting in a significant increase in the power factor. Consequently, numerous research studies have been conducted to synthesize and explore the potential of these organic/inorganic nanocomposites for enhancing thermoelectric performances [17–19]. Most of the composites consist of inorganic fillers, and the fillers in most cases are toxic and perform well only at high temperatures. To overcome these issues, room-temperature and non-toxic inorganic thermoelectric materials (e.g. Bi_2Te_3 [20, 21], Cu_2Se [22]) and their composites (e.g. $Bi_{0.5}Sb_{1.5}Te_3$/PEDOT: PSS [23]) have been explored in recent years. Nevertheless, extensive research is required to enrich the library of room-temperature thermoelectric materials.

Copper iodide (CuI) is an environment-friendly p-type semiconductor compound that exhibits promising Seebeck coefficient at room temperature [24, 25]. Salah et al. reported that Sn-doped CuI exhibited a Seebeck coefficient of 1260 $S·cm^{-1}$ at room temperature [26]. Lately, Xiaowen's group prepared a CuI/nylon film demonstrating a high Seebeck coefficient of 600 $\mu V·K^{-1}$ [27]. On the other hand, PEDOT: PSS is a well-established, highly electrically conductive polymer that has been reported to exhibit an electrical conductivity of 0.8–1418 $S·cm^{-1}$ [28, 29]. However, despite the promising properties of both PEDOT: PSS and CuI, there has been no previous research on the development of PEDOT/CuI nanocomposites for thermoelectric applications. Hence, motivated by the impressive room temperature Seebeck of CuI and the electrical conductivity of PEDOT: PSS, this work sets out to synthesize and

investigate the thermoelectric performance of PEDOT/CuI nanocomposites.

In this work, bulk CuI is prepared from precursors, and then the CuI nanosheets are synthesized by dissolving bulk CuI in DMSO. The PEDOT/CuI nanocomposites are synthesized by physical mixing with ultrasonication. The compositions and the microstructures of the inorganic filler and its nanocomposite films are investigated by X-ray diffraction, scanning electron microscopy (SEM), and transmission electron microscopy (TEM). The effect of CuI fractions on thermoelectric performance is studied. The Seebeck coefficient, electrical conductivity, and power factor are measured by a standard facility called ZEM-3 and the obtained results were used to propose the mechanisms of improved thermoelectrical properties of PEDOT/CuI.

Experimental methods
Materials
PEDOT: PSS solution (1.3 wt%, conductive grade) was purchased from Sigma-Aldrich Pty Ltd. Precursors for copper iodide (CuI), i.e. copper sulphate pentahydrate ($CuSO_4·5H_2O$) and potassium iodide (KI), were supplied by Southern Cross Science Pty Ltd. PVDF membrane (with a nominal pore size of 0.22 μm) and PTFE filter (with a nominal pore size of 0.45 μm) were bought from Proscitech Pty Ltd. All the materials were used without further purification.

Synthesis of bulk CuI
CuI was prepared from precursors by a facile precipitation method based on the following reaction.

$$2 \, CuSO_4 \cdot 5 \, H_2O + 4 \, KI \rightarrow 2 \, CuI \downarrow + I_2 + 2 \, K_2SO_4 + 10 \, H_2O$$
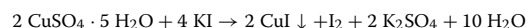
In specific, 655.51 mg of $CuSO_4·5H_2O$ was dissolved in 150 mL of DI water in a beaker by magnetic stirring. In another beaker, a stochiometric quantity of KI was dissolved in 75 mL of DI water by magnetic stirring. After that, the dissolved KI was added dropwise to the first beaker. The precipitation was collected by centrifugation followed by washing with DI water and ethanol for several times to remove K_2SO_4. Finally, bulk CuI particles were dried in a vacuum oven at 60ºC for 8 h.

PEDOT/CuI nanocomposite film fabrication
The preparation procedure of PEDOT/CuI nanocomposites is schematically illustrated in Fig. 1. Aqueous PEDOT: PSS solution was first filtrated with a PTFE membrane to remove large particles. A specific amount of bulk CuI particles (1.9–10.4 vol%) was then added into 20 μL of DMSO, followed by ultrasonication at 200 W for 20 min; 2 mL of DI water was added dropwise, followed by addition of 200 μL of the filtrated PEDOT: PSS. The above
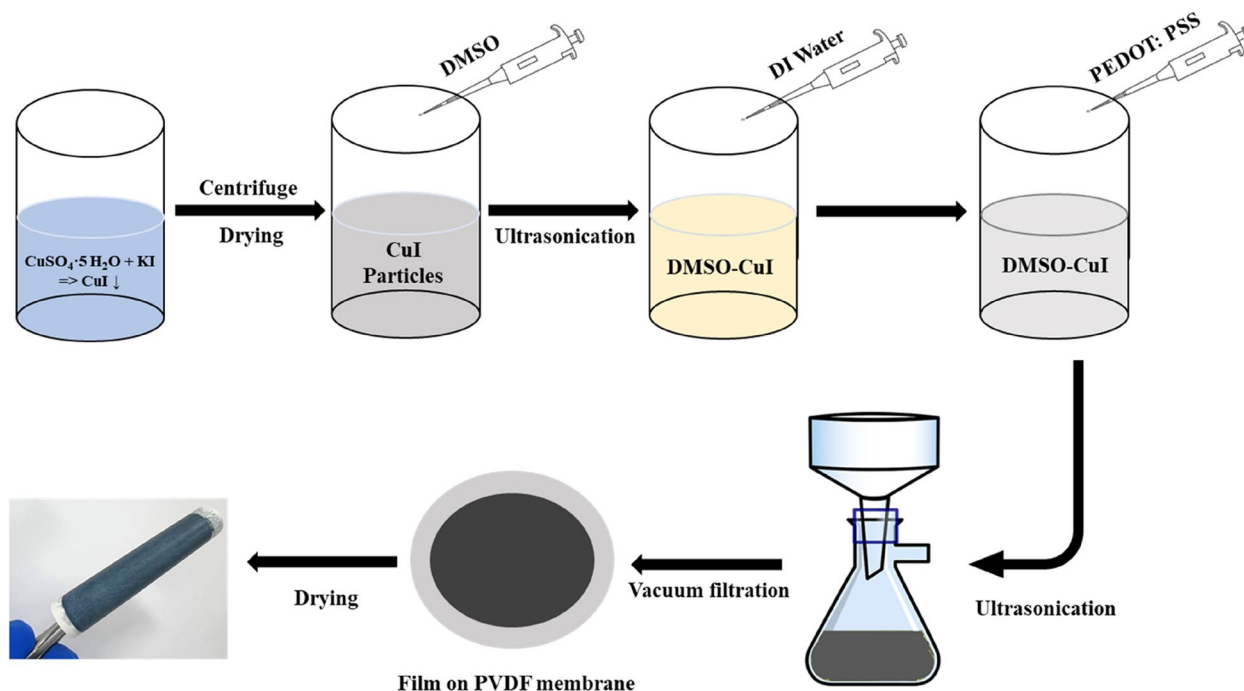
Fig. 1 Schematic representation of the PEDOT/CuI nanocomposite film preparation process

Table 1 Conversion of wt% to vol% of CuI in the PEDOT/CuI nanocomposites

Wt%	9	17	23	29	33	38	41	44	47	50
Vol%	1.9	3.5	4.8	5.9	6.9	7.8	8.6	9.2	9.9	10.4

steps were executed to form nanosized CuI, and the mechanisms will be discussed in detail in the results and discussion section. Afterward, the mixture was further sonicated for 20 min to obtain a visually uniform mixture of CuI and PEDOT: PSS. The mixture was then treated by vacuum filtration on a PVDF membrane, resulting in a PEDOT/CuI nanocomposite film. Finally, the nanocomposite film was dried at 80ºC for 4 h in a vacuum oven prior to characterization and measurement. As will be discussed later, approximately 19.50% of PSS molecules were removed during the filtration and drying process.

To convert wt% to vol%, the densities of CuI and PEDOT: PSS were taken as 5.67 g cm-3 and 1.18 g cm-3. In this way, we converted wt% to vol% as shown in Table 1.

Characterization
X-ray diffraction (XRD) analysis was performed using an Empyrean diffractometer (Malvern PANalytical) with CuKα radiation (wavelength = 1.54 Å) operating at 40 kV and 30 mA. The scanning rate was set at 2°/min,

covering a range of 4–80°. Scherrer's formula was utilized to estimate the crystallite size of the CuI nanosheets from the XRD data. X-ray photoelectron spectroscopy (XPS) measurements were conducted on a Kratos XPS instrument equipped with an Al monochromatic X-ray source (hν = 1486.6 eV) operating at 10 kV. The survey scan was performed with a pass energy of 160 eV, while high-resolution scans utilized a pass energy of 20 eV. The chamber's base pressure during the analysis was maintained at 5.3×10^{-6} Pa. Raman spectra of both the pristine PEDOT: PSS and the PEDOT/CuI nanocomposite were recorded using a HORIBA LabRAM HR Evolution Raman spectrometer. The measurements covered a scan range of 1000-1800 cm^{-1}, and a 532 nm laser was used for excitation. Carrier concentration and mobility were measured using an Ecopia Hall Effect Measurement Systems at room temperature.

Morphology and microstructure analyses were conducted using scanning electron microscopy (SEM) and transmission electron microscopy (TEM). The SEM observations were performed utilizing a Zeiss Merlin
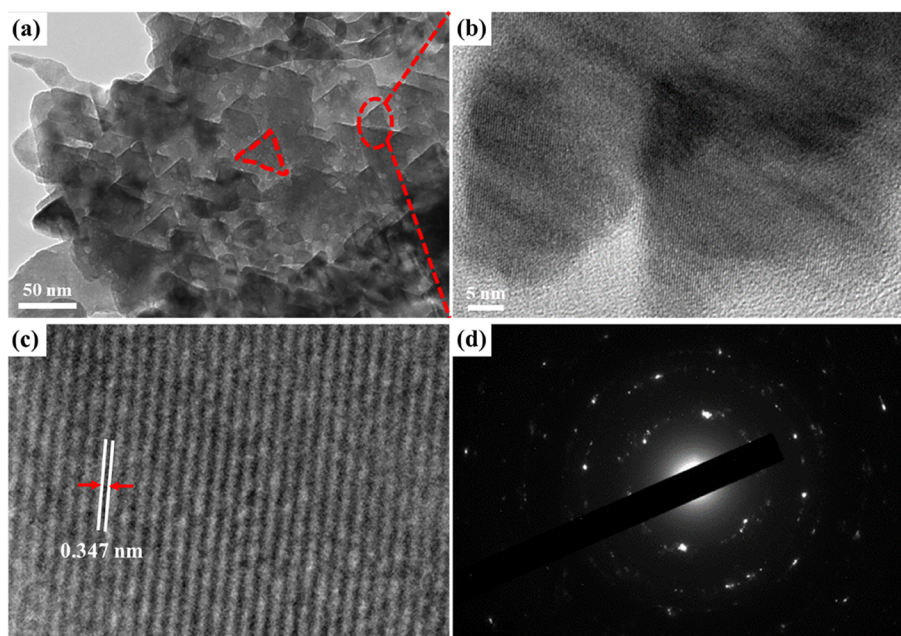
Fig. 2 **a** triangular-like nanosheet structure; **b** HRTEM image, **c** crystalline lattice spacing, and **d** SAED pattern of CuI nanosheets

FEG SEM. Meanwhile, TEM characterization was carried out using a JEOL JEM-2100F-HR instrument. For TEM sample preparation, a 0.02 g DMSO-CuI solution was diluted with 10 mL of ethanol and then subjected to 5 minutes of ultrasonication. This process ensured the uniform dispersion of CuI nanosheets in the solvent, facilitating their successful deposition onto the copper grid with holey carbon support for TEM characterization.

Thermoelectric measurement
A four-point probe method was used to measure the electrical conductivity of all the samples. Temperature-dependant electrical conductivity, Seebeck coefficient, and power factor were measured by a commercial measurement system called "Seebeck Coefficient/Electric Resistance Measuring System (ZEM-3M10, ADVANCE RIKO, Yokohama, Japan)" in He atmosphere, with a test error of ±5%. The thickness of the film on the PVDF membrane was measured by a digital micrometre and an optical microscope. The thickness of the neat PVDF membrane is 100 ± 25 μm, while the pristine and nanocomposite films have thicknesses of 2.7 ± 0.5 μm.

Results and discussion
### Formation of CuI nanosheets
An essential part of this study is to prepare CuI nanosheets. The morphology and the crystallinity of as-prepared CuI nanosheets were studied by TEM and selected area electron diffraction (SAED). As shown in the Fig. 2a, the TEM image of nanosized CuI exhibits a triangular-like nanosheet structure, and the average lateral dimension of the nanosheets is ~33 nm. Further probing of the sample using high-resolution TEM (HRTEM) in Fig. 2b−c shows the presence of crystalline particles with a lattice spacing of 0.347 nm, corresponding to the (1 1 1) plane of CuI (JCPDS no. 06-0246). In addition, Fig. 2d shows the SAED images exhibiting sharp spots, which are due to the crystalline nature of the nanosheets, as supported by a previous work [30].

To verify the successful synthesis of CuI nanosheets, XRD measurement was carried out. The XRD pattern of CuI nanosheets in Fig. 3a is consistent with the pure γ-CuI reported in the literature [31, 32]. Moreover, all the major peaks can be indexed as the standard γ-CuI (JCPDS# 06-0246). High crystallinity of the CuI nanosheets can be demonstrated from the sharp and strong diffraction peaks on the XRD pattern of CuI nanosheets. Using the following Scherrer's formula [23, 24] and all the dominant diffraction peaks from XRD data, we calculated the average crystallite size (d) of as-prepared CuI nanosheets to be ~30 nm, which is close to what we observed under TEM.

$$d = \frac{k\lambda}{\beta \cos\theta}$$

Where λ represents the X-ray wavelength, β means the FWHM width of a diffraction peak, θ refers to the diffraction angle, and k is constant. Table 2 provides the average crystallite size calculated for the as-prepared CuI nanosheets, by utilizing the corresponding peaks, 2-theta
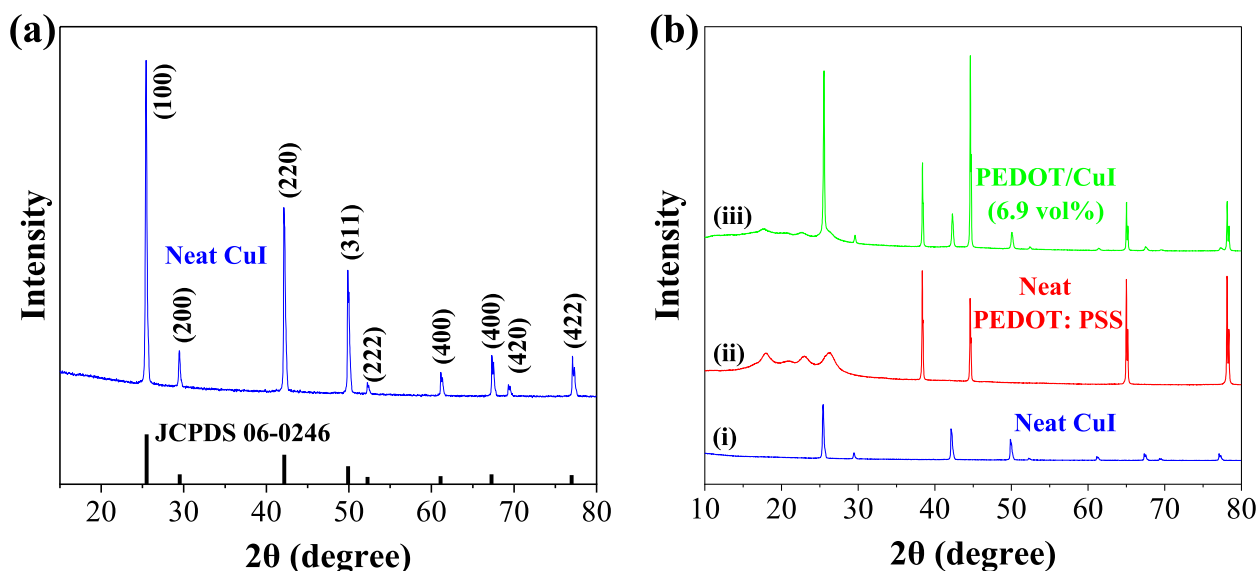
Fig. 3 XRD patterns for **a** as prepared CuI and its corresponding peaks from JCPDS card, and **b** films of neat PEDOT: PSS and PEDOT/CuI nanocomposite at 6.9 vol%

Table 2 Average crystallite size of as-prepared CuI nanosheets

| Peaks	1	2	3	4	5	6	7	8	9	Average size
2-theta	25.44	29.60	42.20	49.95	52.32	61.24	67.44	69.44	77.20	n/a
FWHM	0.22	0.22	0.27	0.30	0.31	0.34	0.37	0.39	0.40	n/a
D (nm)	37.63	37.89	32.10	29.65	28.45	26.87	25.84	24.84	25.19	**~30 nm**

values, FWHM widths, and calculated sizes as reference points.

The formation of CuI nanosheets was explained as below. As discussed in the experiment section, bulk CuI particles were synthesized from precursors. To prepare CuI nanosheets, bulk CuI was dissolved in DMSO by sonication for 20 min, resulting in a CuI-DMSO solution of pale-yellow colour. When DI water was gradually added, CuI nanosheets would be produced through the decomposition of the $[Cu(DMSO)_4]^+$ complex formed in this solution — a passivation layer of Cu^+–DMSO adsorbed on the particle surface was suggested to be responsible for the nanoscale formation. Moreover, DMSO in the solution can still react with the particle surfaces and would act as a capping agent to stabilize each particle by forming a layer of Cu^+–DMSO, preventing them from aggregating. A similar phenomenon was observed when CdS nanoparticles were synthesized in DMSO where the Cd^{2+}–DMSO complex acted as a capping agent for the formation of CdS nanoparticles [33]. Other organic solvents such as dimethyl formamide (DMF) played a similar role in forming CuI nanoparticles [24, 34, 35].

PEDOT/CuI nanocomposites

The dispersion of CuI nanosheets in the PEDOT: PSS matrix was investigated by SEM. Figure 4a–c contains micrographs of the PEDOT/CuI nanocomposite at 1.9 vol%. In Fig. 4a, micron-size clusters and many isolated particles are observed. When magnified in Fig. 4c, the aggregated particles are found to contain a few CuI nanosheets. Figure 4d–f demonstrates similar morphology of the dispersed CuI nanosheets. However, as can be seen in Fig. 4g–i, the morphology of the nanocomposites at 6.9 vol% of CuI shows more aggregated clusters of CuI nanosheets having larger dimensions. Finally, the aggregation in the nanocomposites at 9.2 vol% in Fig. 4j–l seems more severe. Overall, although CuI is well-composited with the PEDOT: PSS matrix, it can clearly be observed that when the fraction of CuI was 6.9 vol% and above, not all particles are properly embedded within the matrix – some sit on the surface of the PEDOT: PSS matrix.

The sample was prepared by cutting with a new razor blade and fracturing at room temperature. Since the matrix has a glass transition temperature far higher than room temperature, the matrix should not deform or deform very little during the sample preparation. The CuI
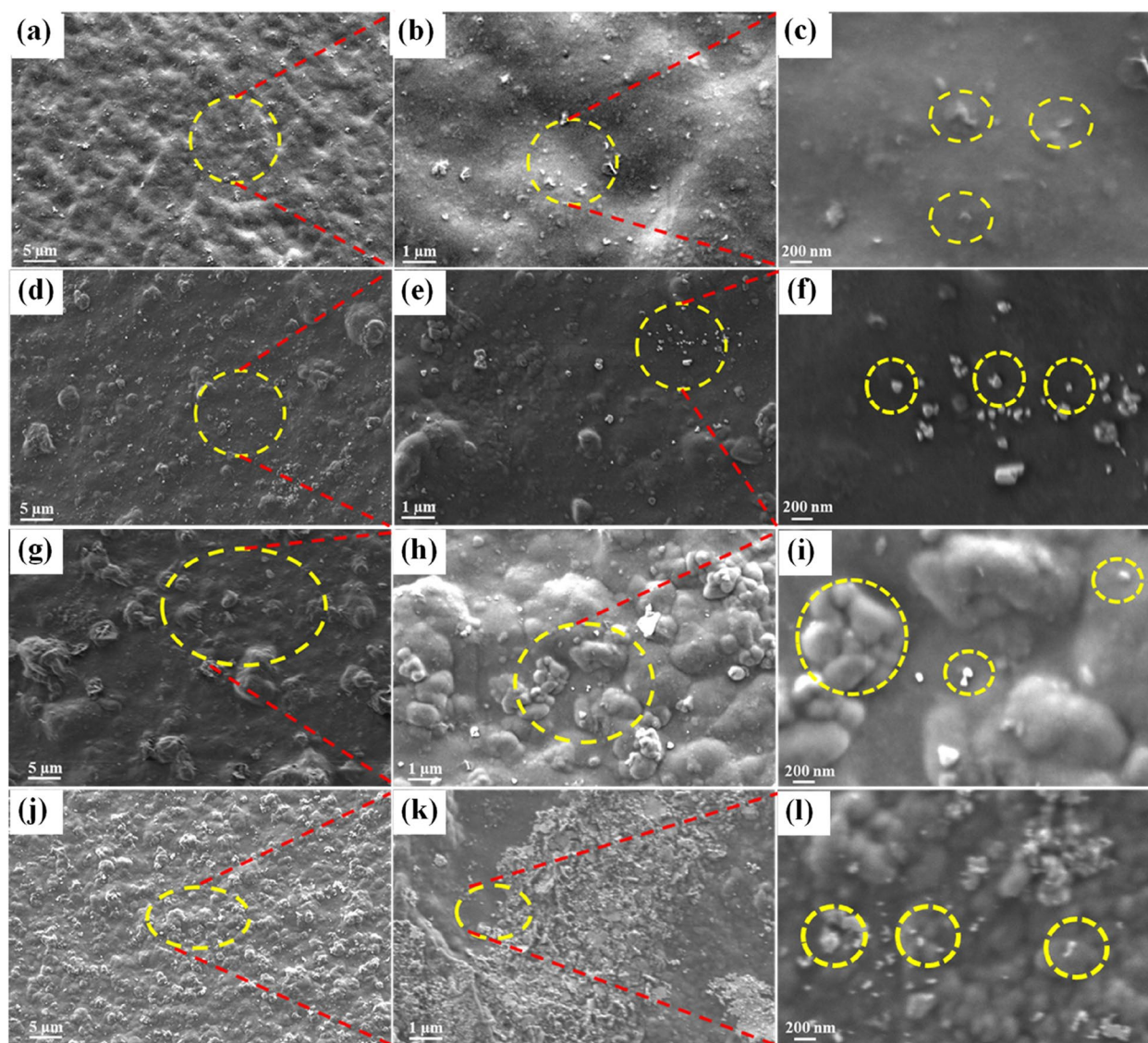
Fig. 4 SEM images of PEDOT/CuI nanocomposites: (**a–c**) 1.9 vol% of CuI, (**d–f**) 4.8 vol%, (**g–i**) 6.9 vol%, and(**j–l**) 9.2 vol%

particles observed on the surface mean that the interfacial bonding between the particles and the matrix is not sufficiently strong. As the CuI fraction increases, many micron-size CuI particles are observed, mainly due to the aggregation of CuI nanosheets via the drying process.

To further confirm the formation of a PEDOT/CuI nanocomposite, EDS analysis was performed. Figure 5a shows a backscattered electron image of the nanocomposite film. During the EDS measurement, different areas were focused, and the corresponding peak of one such area is shown in Fig. 5b. All the elements from PEDOT: PSS (e.g., C and S) and CuI (Cu and I) can be seen in the synthesized nanocomposite in the EDS spectrums. In addition, the EDS mapping shown in Fig. 5c-g also

indicates the presence of S, C, Cu, and I. The I/Cu atom ratio in the nanocomposite film was calculated to be 1.28, which reasonably agrees with the stoichiometric ratio in CuI.

Moreover, XRD analysis was performed to further characterize the nanocomposite as briefly discussed in Fig. 3. Figure 3b illustrates the XRD pattern of the nanocomposite at 6.9 vol%, and it exhibits diffraction peaks that appear to be a combination of the patterns observed for both CuI nanosheets and neat PEDOT: PSS. The overlapping peaks indicate successful dispersion and integration of CuI nanosheets into the PEDOT: PSS matrix. As summarized in Table S1, shifts in peak positions and changes in intensities at specific 2θ angles, such as at $2\theta = 18.28$ and 26.44

Alam *et al. Functional Composite Materials* (2023) 4:9

Page 8 of 13
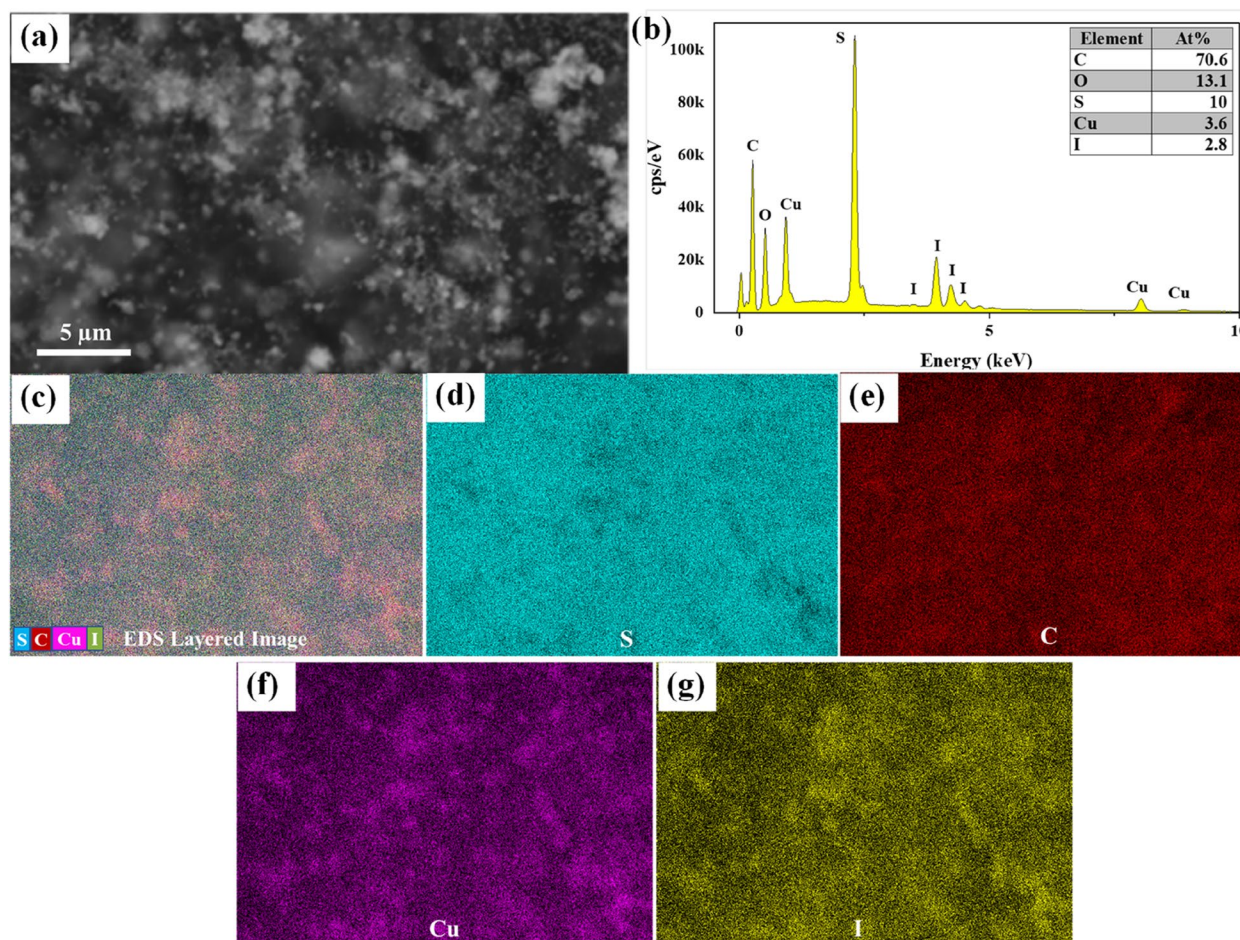
Fig. 5 **a** Backscattered electron image with **b** atomic percentage; EDS mapping showing (**c**) layered image, and the distribution of **d** sulfur, **e** carbon, **f** copper, and **g** iodine within the nanocomposite

degrees, suggest structural modifications resulting from the interaction between CuI nanosheets and PEDOT: PSS. The preservation of certain characteristic peaks at $2\theta = 4.04$, 44.62, 65.00, and 78.12 degrees further confirms the successful formation of the nanocomposite, with CuI nanosheets distributed within the PEDOT: PSS matrix. These XRD findings provide strong evidence for the effective synthesis of the PEDOT/CuI nanocomposite, showcasing its distinctive crystalline features and successful incorporation of CuI nanosheets within the PEDOT: PSS matrix.

## Thermoelectric performance of PEDOT/CuI nanocomposite film

Figure 6a shows the electrical conductivity of the PEDOT/CuI nanocomposite film at CuI fractions ranging from 0–10.4 vol%. Initially, the DMSO-treated PEDOT: PSS film exhibits a conductivity of approximately 9.0 S·cm^{-1} at room temperature. However, the addition of CuI nanosheets leads to a notable increase in electrical

conductivity. For example, the conductivity increases from 35 ± 19 S·cm^{-1} at 1.9 vol% of CuI to a maximum value of 852 ± 195 S·cm^{-1} at 6.9 vol%. A similar increase was reported for PEDOT: PSS compounded with Bi$_2$Te$_3$ [36, 37]. This conductivity improvement is explained below.

Firstly, DMSO, an organic solvent, weakens the coulombic interaction between PEDOT (+) and PSS (-), resulting in increased electrical conductivity of PEDOT: PSS due as supported by [38]. Moreover, adding CuI nanosheets could create a conformational change to the PEDOT chains and also provide carriers for PEDOT: PSS to attach [37]. As a result, PEDOT macromolecules would change from coiled to linear structure, making the charge carriers move along the polymer chains more efficiently, as illustrated in Fig. 6e.

However, the conductivity decreases at higher CuI fractions (above 6.9 vol%). The reduction can be attributed to the less effective dispersion of CuI nanosheets due to the
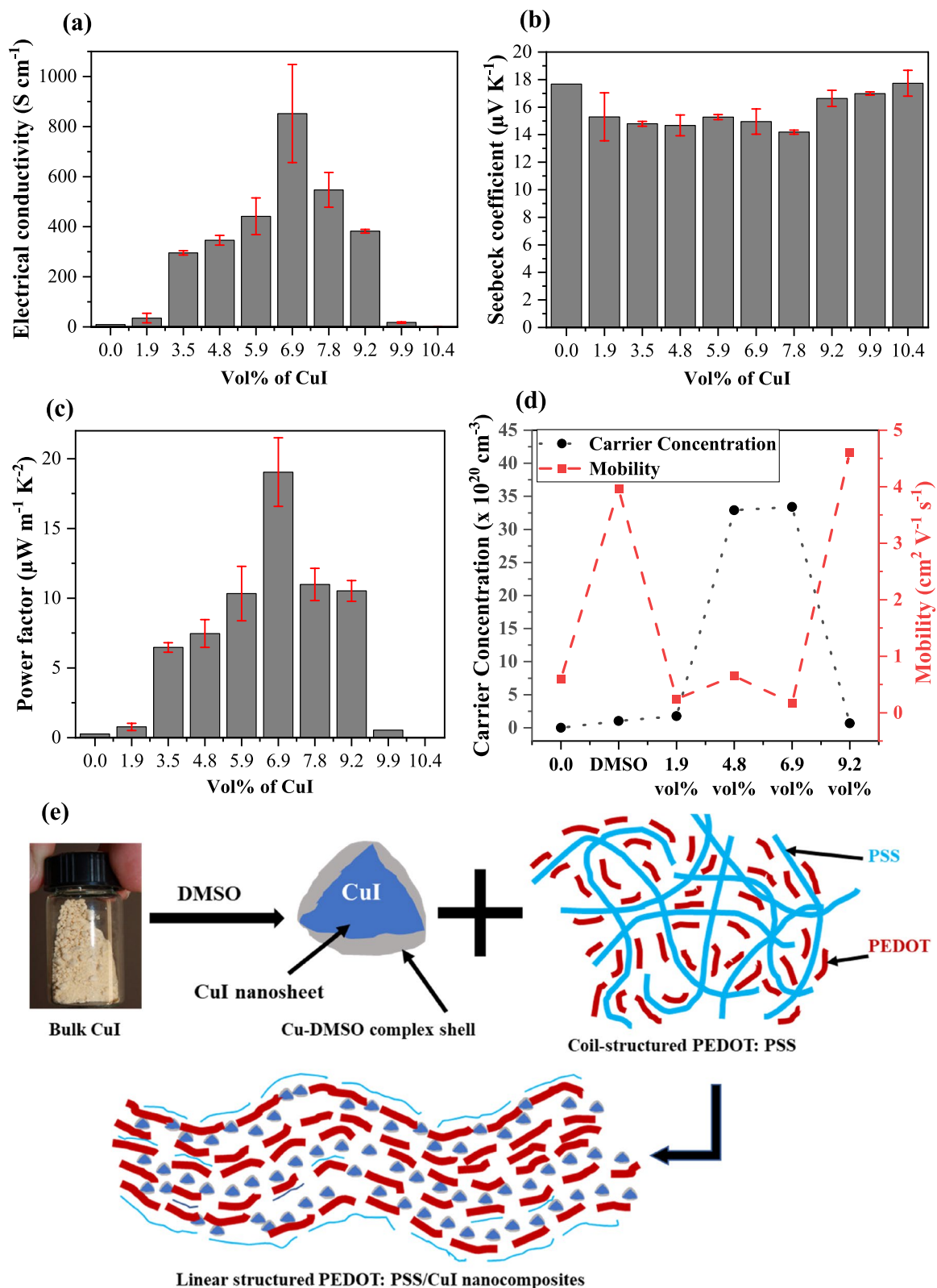
Fig. 6 **a** Electrical conductivity, **b** Seebeck coefficient, **c** power factor, **d** carrier concentrations and mobility of PEDOT: PSS and PEDOT/CuI; and (**e**) the formation process of linear structured PEDOT/CuI

excess amount of CuI in the matrix, which would result in fewer "accelerator" loci, making the charge carrier transport more challenging [39]; that is, excessive CuI nanosheets act as a barrier between conductive PEDOT chains, decreasing the conductivity.

To investigate whether DMSO and CuI nanosheets pose an effect on the inner composition of the PEDOT: PSS film, X-ray photoelectron spectroscopy (XPS) measurements were performed. The S(2p) XPS spectra of neat PEDOT: PSS and its nanocomposite films are compared in Fig. 7a. Neat PEDOT: PSS exhibits two signal bands at 158−162 (doublet peaks) and 162−166 eV, which are assigned to the sulphur atoms of PEDOT and PSS, respectively. The use of DMSO and CuI has shifted the peaks a little bit to the lower energy and strengthened the signals of both PEDOT and PSS chains, indicating that the PEDOT and PSS chains are more separated.

The possible compositional change in the nanocomposite films is probed by the PEDOT-to-PSS ratio calculated according to the integrated peak areas of the S(2p) [40], as summarised in Table 3.

Table 3 Ratios of PSS to PEDOT from the area under XPS graphs

Sample	PEDOT area	PSS area	PSS to PEDOT
Pristine PEDOT: PSS	0.05437	0.12111	2.2275
DMSO-PEDOT: PSS	0.06286	0.13038	2.0741
PEDOT/CuI (1.9 vol%)	0.00597	0.1272	1.8847
PEDOT/CuI (4.8 vol%)	0.06412	0.1186	1.8493
PEDOT/CuI (6.9 vol%)	0.0654	0.1173	1.7934
PEDOT/CuI (9.2 vol%)	0.0642	0.1147	1.7975
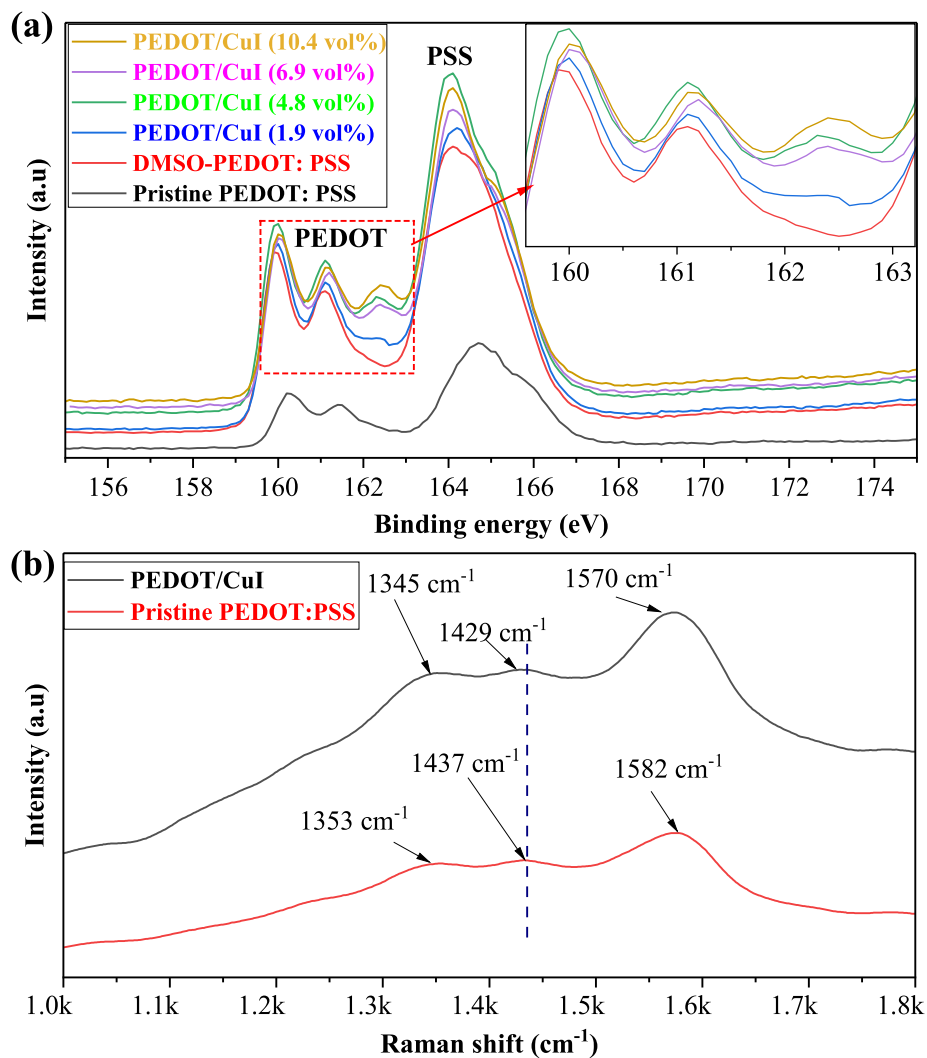
Fig. 7 **a** S(2p) XPS spectra, and **b** Raman spectra of PEDOT: PSS and PEDOT/CuI

Normalized XPS data was used to evaluate the PSS to PEDOT ratio for PEDOT: PSS and its composites. Although UV-vis spectroscopy was also found useful in this regards as reported by Mardi et al [41], XPS is more often used due to higher accuracy [42, 43]. In Table 3, the ratio of PSS to PEDOT reduces as the CuI fraction increases. For the pristine polymers, the ratio was measured as 2.2275. When DMSO was used with CuI nanosheets added, the ratio started to reduce down to 1.7934 for the nanocomposite at 6.9 vol% of CuI. These results suggest that the nanocomposite composition has evolved during the preparation, likely corresponding to removal of a considerable amount (around 19.50%) of PSS component from PEDOT: PSS. This eventually resulted in an improvement in the electrical conductivity of the nanocomposite film. Nevertheless, the PSS to PEDOT ratios of the nanocomposite films tend to stop decreasing at over 6.9 vol% of CuI. This result is consistent with the trend of electrical conductivity in Fig. 6a.

Raman analysis has been employed to investigate the conformational change in the structure of PEDOT chains. In Fig. 7b, the peaks for the PEDOT/CuI nanocomposite are slightly shifted towards the red region in comparison with those for PEDOT: PSS. The shift indicates a conformational change in the structure of the PEDOT chains from a coiled to an extended coiled or linear structure [44, 45]. This change is likely due to the presence of both the CuI nanosheets and DMSO. The linear structure of the PEDOT chains is known to have a positive effect on the electrical conductivity of their nanocomposite [46]. Additionally, the XRD patterns in Fig. 3b indicate noticeable changes in the crystallization or arrangement of PEDOT and PSS chains in the nanocomposite film. Although the XRD patterns for the nanocomposite film are observed at similar positions to pristine PEDOT: PSS, the pattern intensities are significantly altered. A summary of the intensity and peak position changes can be found in Table S1. These changes in the XRD and Raman data suggest that the PEDOT macromolecules have undergone a conformational change from a coiled to a linear structure in the nanocomposite.

Hall measurements were performed to investigate the charge carrier concentrations and mobility of the nanocomposites. In Fig. 6d the carrier concentration increases with the CuI fractions up to 6.9 vol%, indicating the beneficial effect of CuI in enhancing the number of charge carriers available for conduction. This increase in carrier concentration contributed significantly to the observed enhancement in electrical conductivity.

However, the carrier concentration at 9.2 vol% of the nanosheets decreases compared to the 6.9 vol%. It is attributed to the formation of large clusters or agglomerates of CuI nanosheets, hindering the efficient interaction between PEDOT and CuI, thus impeding the charge transport.

On the other hand, the carrier mobility exhibits varying behavior with CuI fractions. The presence of numerous heterointerfaces and different phases in the nanocomposites would influence the mobility of charge carriers, leading to variations in transport behavior. Some nanocomposites show a decrease in mobility, while others display an increase.

Considering these findings, we affirm that the addition of CuI nanosheets to the PEDOT: PSS matrix significantly enhanced the electrical conductivity through both the increase in carrier concentration and the formation of a conductive network within the matrix. The use of DMSO treatment also plays a crucial role in the conductivity improvement.

Regarding the Seebeck coefficient, the nanocomposite films exhibited a slight fluctuation in the range of 14.1 to 18.4 $\mu V \cdot K^{-1}$ with varying fractions of CuI nanosheets. In Fig. 6b, the DMSO-treated PEDOT: PSS film exhibits a Seebeck coefficient value of 17.7 $\mu V \cdot K^{-1}$, whereas the nanocomposite film with 6.9 vol% of CuI nanosheets shows 14.95 $\mu V \cdot K^{-1}$. The maximum value of 18.4 $\mu V \cdot K^{-1}$ is exhibited by the nanocomposite with 10.4 vol% of CuI nanosheets. These values are lower in comparison with the Seebeck coefficient of our neat CuI film which was measured as 194 $\mu V \cdot K^{-1}$ at room temperature. A similar phenomenon was reported by [36, 37, 47] when Bi_2Te_3 was composited with PEDOT: PSS. The reason was attributed to that the electrically connecting junctions between the Bi_2Te_3 particles were weakened or destroyed, resulting in no obvious enhancement of the Seebeck coefficient for the PEDOT: PSS nanocomposite films containing Bi_2Te_3. Our group is currently investigating novel strategies to further enhance the Seebeck coefficient of the nanocomposite film.

Figure 6c contains the power factors of PEDOT: PSS and its nanocomposite films. At room temperature, the DMSO-treated PEDOT: PSS film without CuI shows a power factor of 0.27 $\mu W \cdot m^{-1} \cdot K^{-2}$. As the CuI nanosheets are added, the power factor gradually increases, reaching a peak at 6.9 vol% of CuI nanosheets. However, beyond this concentration, the power factor starts to decrease, reaching 11 ± 1.15 $\mu W \cdot m^{-1} \cdot K^{-2}$ at 7.8 vol%. Since the power factor is calculated by $PF = S^2\sigma$ and Seebeck coefficient remains relatively stable with the CuI fraction, the electrical conductivity of the nanocomposite films plays a crucial role in determining the power factor. Therefore, the nanocomposite film containing 6.9 vol% of CuI exhibits the highest power factor with a mean value of 19.04 $\mu W \cdot m^{-1} \cdot K^{-2}$, corresponding to the highest electrical conductivity of 852.07 $S \cdot cm^{-1}$. This performance is compared with similar nanocomposites

Alam *et al. Functional Composite Materials*   (2023) 4:9

Page 12 of 13

that utilize non-toxic elements and avoid post-treatment. The results show comparable performance, as presented in Table S2 in the supplementary document.

Conclusion

In conclusion, flexible thermoelectric PEDOT/CuI nanocomposite films were prepared by vacuum filtration on a PVDF membrane. The CuI nanosheets, synthesized from non-toxic precursors, were incorporated into the PEDOT: PSS matrix using ultrasonication. The broad range of CuI concentrations (1.9–10.4 vol%) in nanocomposite film was explored, where the nanocomposite film with 6.9 vol% CuI nanosheets exhibited optimal performance. Despite its relatively low Seebeck coefficient of 14.95 $\mu V \cdot K^{-1}$, the nanocomposite exhibited an enhanced power factor of 19.04 $\mu W \cdot m^{-1} \cdot K^{-2}$ at room temperature, surpassing the performance of the individual constituents of the nanocomposite. This enhancement in the power factor can be attributed to the improved electrical conductivity of 852.07 $S \cdot cm^{-1}$. These findings on PEDOT/CuI nanocomposite films as new thermoelectric nanocomposites are showing promising results that would advance research in the field of polymer/inorganic nanocomposites for thermoelectric applications.

Supplementary Information

The online version contains supplementary material available at https://doi.org/10.1186/s42252-023-00047-x.

Additional file 1: Table S1. Comparison of intensity and peak position in XRD patterns between pristine PEDOT: PSS and its nanocomposite. **Table S2.** TE performance of PEDOT: PSS-based organic-inorganic nanocomposites.

Authors' contributions
JA led the writing. XS contributed to the testing data. SA and KZ verified the analytical methods. QM and FM contributed to the theory development. DL and JM contributed to the funding. JA and JM conceived of the presented idea.

Availability of data and materials
All the data generated or analyzed during this study are included in this manuscript.

Declarations

Competing interests
The authors declare no competing interests.

Author details
[1]UniSA STEM and Future Industries Institute, University of South Australia, Adelaide, SA 5095, Australia. [2]Department of Chemical and Materials Engineering, Southern Taiwan University of Science and Technology, Tainan City 710301, Taiwan. [3]College of Aerospace Engineering, Shenyang Aerospace University, Shenyang 110136, China. [4]The ARC Graphene Research Hub, School of Chemical Engineering and Advanced Materials, The University of Adelaide, Adelaide, SA 5005, Australia.

References
1. K. Koumoto, I. Terasaki, R. Funahashi, Complex Oxide Materials for Potential Thermoelectric Applications. MRS Bulletin **31**(3), 206–210 (2006). https://doi.org/10.1557/mrs2006.46
2. LLNL. World Energy Flow Chart. 2014; Available from: https://flowcharts.llnl.gov/
3. M.S. Dresselhaus et al., New directions for low-dimensional thermoelectric materials. Adv Mater **19**(8), 1043–1053 (2007). https://doi.org/10.1002/adma.200600527
4. P. Li et al., Facile green strategy for improving thermoelectric performance of carbon nanotube/polyaniline composites by ethanol treatment. Compos Sci Technol **189**, 108023 (2020). https://doi.org/10.1016/j.compscitech.2020.108023
5. G. Prunet et al., A review on conductive polymers and their hybrids for flexible and wearable thermoelectric applications. Mater Today Phys **18**, 100402 (2021). https://doi.org/10.1016/j.mtphys.2021.100402
6. X.-L. Shi, J. Zou, Z.-G. Chen, Advanced Thermoelectric Design: From Materials and Structures to Devices. Chem Rev **120**(15), 7399–7515 (2020). https://doi.org/10.1021/acs.chemrev.0c00026
7. L.-D. Zhao et al., Ultralow thermal conductivity and high thermoelectric figure of merit in SnSe crystals. Nature **508**(7496), 373–377 (2014). https://doi.org/10.1038/nature13184
8. F. Meng et al., Bismuthene Nanosheets Prepared by an Environmentally Friendly Method and Their Thermoelectric Epoxy Nanocomposites. Adv Ind Eng Polymer Res (2023). https://doi.org/10.1016/j.aiepr.2023.06.003
9. Q. Meng et al., Preparation of antimonene nanosheets and their thermoelectric nanocomposites. Compos Commun **28**, 100968 (2021). https://doi.org/10.1016/j.coco.2021.100968
10. Z. Yang et al., Free-standing PEDOT/polyaniline conductive polymer hydrogel for flexible solid-state supercapacitors. Electrochimica Acta **322**, 134769 (2019). https://doi.org/10.1016/j.electacta.2019.134769
11. M. Moussa et al., Development of flexible supercapacitors using an inexpensive graphene/PEDOT/MnO2 sponge composite. Mater Design **125**, 1–10 (2017). https://doi.org/10.1016/j.matdes.2017.03.075
12. Z. Zhao et al., PEDOT-based composites as electrode materials for supercapacitors. Nanotechnology **27**(4), 042001 (2016). https://doi.org/10.1088/0957-4484/27/4/042001
13. N. Toshima, S. Ichikawa, Conducting polymers and their hybrids as organic thermoelectric materials. J Electron Mater **44**(1), 384–390 (2015). https://doi.org/10.1007/s11664-014-3312-1
14. H. Ju, J. Kim, Chemically Exfoliated SnSe Nanosheets and Their SnSe/Poly(3,4-ethylenedioxythiophene):Poly(styrenesulfonate) Composite Films for Polymer Based Thermoelectric Applications. ACS NANO **10**(6), 5730–5739 (2016). https://doi.org/10.1021/acsnano.5b07355
15. Bae, E.J., et al., Enhancement of Thermoelectric Properties of PEDOT:PSS and Tellurium-PEDOT:PSS Hybrid Composites by Simple Chemical Treatment. SCIENTIFIC REPORTS, 2016. **6** https://doi.org/10.1038/srep18805
16. K.C. See et al., Water-Processable Polymer-Nanocrystal Hybrids for Thermoelectrics. Nano Lett **10**(11), 4664–4667 (2010). https://doi.org/10.1021/nl102880k
17. Y. Du et al., Facile preparation and thermoelectric properties of Bi2Te3 based alloy nanosheet/PEDOT: PSS composite films. ACS Appl Mater Interfaces **6**(8), 5735–5743 (2014). https://doi.org/10.1021/am5002772
18. J. Gainza et al., High-Performance n-type SnSe Thermoelectric Polycrystal Prepared by Arc-Melting. Cell Rep Physic Sci **1**(12), 100263 (2020). https://doi.org/10.1016/j.xcrp.2020.100263

19. Z.-H. Ge et al., Improved thermoelectric properties of PEDOT: PSS polymer bulk prepared using spark plasma sintering. Chem Commun **54**(19), 2429–2431 (2018). https://doi.org/10.1039/C7CC09595C

20. D. Bao et al., Texture-dependent thermoelectric properties of nano-structured Bi2Te3. Chem Eng J **388**, 124295 (2020). https://doi.org/10.1016/j.cej.2020.124295

21. Y. Wang et al., Enhanced thermoelectric properties of nanostructured n-type Bi2Te3 by suppressing Te vacancy through non-equilibrium fast reaction. Chem Eng J **391**, 123513 (2020). https://doi.org/10.1016/j.cej.2019.123513

22. W.-W. Liao et al., Realizing Bi-doped α-Cu2Se as a promising near-room-temperature thermoelectric material. Chem Eng J **371**, 593–599 (2019). https://doi.org/10.1016/j.cej.2019.04.081

23. Y. Wang et al., Bi0. 5Sb1. 5Te3/PEDOT: PSS-based flexible thermoelectric film and device. Chem Eng J **397**, 125360 (2020). https://doi.org/10.1016/j.cej.2020.125360

24. Y. Yang, S. Liu, K. Kimura, Synthesis of Well-dispersed CuI Nanoparticles from an Available Solution Precursor. Chemistry Letters **34**(8), 1158–1159 (2005). https://doi.org/10.1246/cl.2005.1158

25. C. Yang et al., Transparent flexible thermoelectric material based on non-toxic earth-abundant p-type copper iodide thin film. Nat Commun **8**(1), 1–7 (2017). https://doi.org/10.1038/ncomms16076

26. N. Salah et al., Effective dopants for CuI single nanocrystals as a promising room temperature thermoelectric material. Ceram Int **46**(17), 27244–27253 (2020). https://doi.org/10.1016/j.ceramint.2020.07.209

27. X. Han et al., CuI/Nylon Membrane Hybrid Film with Large Seebeck Effect. Chin Phys Lett **38**(12), 126701 (2021). https://doi.org/10.1088/0256-307X/38/12/126701

28. Y. Shi et al., Solution-based synthesis of PEDOT:PSS films with electrical conductivity over 6300 S/cm. J Ind Eng Chem **101**, 414–422 (2021). https://doi.org/10.1016/j.jiec.2021.05.036

29. N.A.A. Shahrim et al., Mechanisms for doped PEDOT:PSS electrical conductivity improvement. Mat Adv **2**(22), 7118–7138 (2021). https://doi.org/10.1039/D1MA00290B

30. V. Parashar et al., Parthenium leaf extract mediated synthesis of silver nanoparticles: a novel approach towards weed utilization. Dig J Nanomat Biostruct **4**(1), 45–50 (2009)

31. K. Yao et al., Synthesis of ultrathin two-dimensional nanosheets and van der Waals heterostructures from non-layered γ-CuI. npj 2D Mat Appl **2**(1), 16 (2018). https://doi.org/10.1038/s41699-018-0058-2

32. C.H.B. Ng, W.Y. Fan, Facile Synthesis of Single-Crystalline γ-CuI Nanotetrahedrons and Their Induced Transformation to Tetrahedral CuO Nanocages. J Phys Chem C **111**(26), 9166–9171 (2007). https://doi.org/10.1021/jp071773d

33. M.E. Wankhede, S.K. Haram, Synthesis and Characterization of Cd─DMSO Complex Capped CdS Nanoparticles. Chem Mater **15**(6), 1296–1301 (2003). https://doi.org/10.1021/cm020761w

34. Y. Zhong et al., Enhancing Efficiency and Stability of Polymer Solar Cells Based on CuI Nanoparticles as the Hole Transport Layer. IEEE J Photovoltaics **11**(3), 668–673 (2021). https://doi.org/10.1109/JPHOTOV.2021.3064575

35. M.R. Johan et al., Synthesis and Characterization of Copper (I) Iodide Nanoparticles via Chemical Route. Int J Electrochem Sci **7**(6), 4942–4950 (2012)

36. H. Song et al., Improved Thermoelectric Performance of Free-Standing PEDOT:PSS/Bi2Te3 Films with Low Thermal Conductivity. J Electronic Mater **42**(6), 1268–1274 (2013). https://doi.org/10.1007/s11664-013-2587-y

37. M. Bharti et al., Boosting thermoelectric power factor of free-standing Poly(3,4ethylenedioxythiophene):polystyrenesulphonate films by incorporation of bismuth antimony telluride nanostructures. Journal of Power Sources **435**, 226758 (2019). https://doi.org/10.1016/j.jpowsour.2019.226758

38. J.Y. Kim et al., Enhancement of electrical conductivity of poly(3,4-ethylenedioxythiophene)/poly(4-styrenesulfonate) by a change of solvents. Synthetic Metals **126**(2–3), 311–316 (2002). https://doi.org/10.1016/S0379-6779(01)00576-8

39. Y. Ma, W. Wijesekara, A.E.C. Palmqvist, Electrochemical Deposition and Characterization of Thermoelectric Ternary (BixSb1─x)2Te3 and Bi2(Te1─ySey)3 Thin Films. J Electron Mater **41**(6), 1138–1146 (2012). https://doi.org/10.1007/s11664-011-1790-y

40. S.-I. Na et al., Evolution of nanomorphology and anisotropic conductivity in solvent-modified PEDOT:PSS films for polymeric anodes of polymer solar cells. J Mater Chem **19**(47), 9045–9053 (2009). https://doi.org/10.1039/B915756E

41. S. Mardi et al., The Interfacial Effect on the Open Circuit Voltage of Ionic Thermoelectric Devices with Conducting Polymer Electrodes. Adv Electron Mater **7**(12), 2100506 (2021). https://doi.org/10.1002/aelm.202100506

42. R. Chen et al., PEDOT:PSS as Stretchable Conductors with Good Wettability on the Substrate through the Simultaneous Plasticization and Secondary Doping with a Cationic or Anionic Surfactant. Macromolecules **55**(12), 4967–4978 (2022). https://doi.org/10.1021/acs.macromol.2c00592

43. T. Horii et al., Correlation between the hierarchical structure and electrical conductivity of PEDOT/PSS. Polymer J **47**(10), 695–699 (2015). https://doi.org/10.1038/pj.2015.48

44. Xu, B., et al. Improving Air-Stability and Performance of Bulk Heterojunction Polymer Solar Cells Using Solvent Engineered Hole Selective Interlayer. Materials, 2018. **11** https://doi.org/10.3390/ma11071143

45. H.J. Oh et al., Structural and Morphological Evolution for Water-resistant Organic Thermoelectrics. Sci Rep **7**(1), 13287 (2017). https://doi.org/10.1038/s41598-017-13726-0

46. Q. Meng et al., Preparation and thermoelectric properties of PEDOT:PSS coated Te nanorod/PEDOT:PSS composite films. Organic Electron **64**, 79–85 (2019). https://doi.org/10.1016/j.orgel.2018.10.010

47. H. Song, K. Cai, Preparation and properties of PEDOT:PSS/Te nanorod composite films for flexible thermoelectric power generator. Energy **125**, 519–525 (2017). https://doi.org/10.1016/j.energy.2017.01.037

Publisher's Note